

# Spatiotemporal Calibration of 3D mm-Wavelength Radar-Camera Pairs

Emmett Wise, Qilong Cheng, and Jonathan Kelly

**Abstract**—Autonomous vehicles (AVs) often depend on multiple sensors and sensing modalities to mitigate data degradation and provide a measure of robustness when operating in adverse conditions. Radars and cameras are a popular sensor combination—although radar measurements are sparse in comparison to camera images, radar scans are able to penetrate fog, rain, and snow. Data from both sensors are typically fused prior to use in downstream perception tasks. However, accurate sensor fusion depends upon knowledge of the spatial transform between the sensors and any temporal misalignment that exists in their measurement times. During the life cycle of an AV, these calibration parameters may change. The ability to perform in-situ spatiotemporal calibration is essential to ensure reliable long-term operation. State-of-the-art 3D radar-camera spatiotemporal calibration algorithms require bespoke calibration targets that are not readily available in the field. In this paper, we describe an algorithm for *targetless* spatiotemporal calibration that is able to operate without specialized infrastructure. Our approach leverages the ability of the radar unit to measure its own ego-velocity relative to a fixed external reference frame. We analyze the identifiability of the spatiotemporal calibration problem and determine the motions necessary for calibration. Through a series of simulation studies, we characterize the sensitivity of our algorithm to measurement noise. Finally, we demonstrate accurate calibration for three real-world systems, including a handheld sensor rig and a vehicle-mounted sensor array. Our results show that we are able to match the performance of an existing, target-based method, while calibrating in arbitrary (infrastructure-free) environments.

**Index Terms**—Calibration & Identification, Sensor Fusion, Robot Sensing Systems, Radar, Computer Vision

## I. INTRODUCTION

The widespread deployment of autonomous vehicles (AVs) depends critically on their ability to operate safely under a range of challenging environmental conditions. For this reason, most AV perception systems incorporate multiple sensors and sensing modalities to ensure sufficient redundancy. In this paper, we consider 3D mm-wavelength radar as a complementary sensor to standard cameras for safe AV perception.

The operating principle of mm-wavelength radars (i.e., the active emission of mm-wavelength electromagnetic radiation) makes these sensors relatively immune to adverse conditions that negatively affect cameras. Radars also provide information that cameras do not, including *range rate* measurements of

Emmett Wise, Qilong Cheng, and Jonathan Kelly are with the Space and Terrestrial Autonomous Robotic Systems Laboratory, University of Toronto, Institute for Aerospace Studies, Toronto, Canada. {<first name>.<last name>@robotics.utias.utoronto.ca}

This work was supported in part by the Natural Sciences and Engineering Research Council of Canada (NSERC). The work of Jonathan Kelly was supported by the Canada Research Chairs Program. Jonathan Kelly is a Vector Institute Faculty Affiliate.

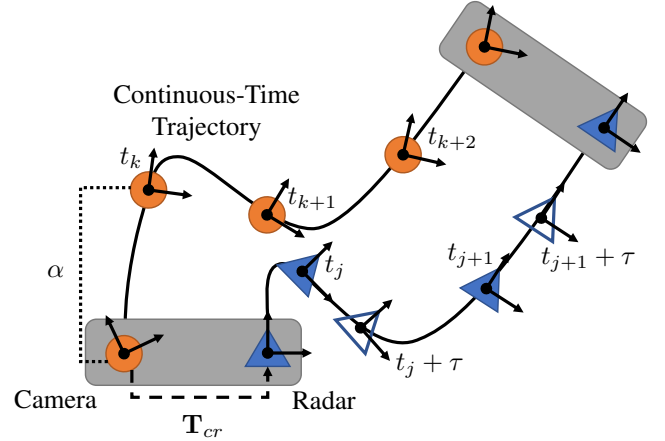


Fig. 1: The radar (triangle) and camera (circle) are assumed to be rigidly connected. Our calibration problem involves estimating the transform between the camera and radar,  $T_{cr}$ , the translation scale factor,  $\alpha$ , for the camera pose measurements, and the temporal offset,  $\tau$ . The unfilled triangles represent radar measurements at “shifted” points in time due to the offset bias. The radar ego-velocity estimate will not be correct unless this bias is considered.

the relative velocity of targets in the environment. However, radar data are much lower resolution, and are significantly more noisy, than visual measurements under nominal conditions. Together, radars and cameras are highly complementary, providing situational awareness under nominal and visually-degraded conditions.

To be used jointly in the AV perception stack, radar and camera sensors must be calibrated with respect to each other. The spatial (6-DoF) transform between a radar-camera pair must be known accurately in order to express the data in a common reference frame. An AV may undergo calibration ‘at the factory’ prior to operation, but maintenance and general wear and tear can alter the spatial calibration parameters. Further improvements in performance are possible when the sensor data streams are temporally aligned also. Even when the sensors are externally triggered, internal signal processing delays can result in shifted measurement timestamps. If this time offset is not accounted for, then, for example, moving targets will be *spatially* shifted in the radar and camera measurements. Further, in some systems, power cycling or reconfiguring the sensors may change the time offset. As a result, temporal calibration may need to be performed routinely to ensure the accuracy and integrity of fused sensor data.

An in-situ method to estimate the spatial transformation between the radar and camera, and the temporal offset of

the sensor data streams, would enable long-term AV operation in the field. However, existing radar-camera spatial and spatiotemporal calibration algorithms are restricted to certain environments and sensor configurations [1] [2]. Primarily, these methods rely on the assumption that the radar measures ‘point-like’ reflections from objects. In general, a radar measurement (of the reflected electromagnetic pulse) is a complex function of the shape, relative orientation, size, and composition of an object [3]. An additional difficulty is that multipath reflections can produce outlier measurements of ghost ‘objects’ [3]. To avoid these problems, specialized trihedral retroreflective radar targets are used to produce the desired point-like radar returns. A visual fiducial can be placed over or alongside the trihedral target, allowing radar-camera measurement correspondences to be established. The use of targets, however, means that calibration must be carried out in specialized areas or with infrastructure that is not usually available during regular AV operation. Additionally, the algorithms require that the radar-camera pair(s) share overlapping fields of view, which may not be possible for all radar-camera systems.

Herein, we extend the method in [4] to jointly estimate the extrinsic calibration parameters and temporal offset of a 3D mm-wavelength radar-camera pair in a fully targetless manner. Importantly, our approach does not require the sensors to share overlapping fields of view. Instead, we use the radar measurements to estimate the instantaneous radar ego-velocity, that is, the velocity of the radar unit relative to an external reference frame, expressed in the radar reference frame [5]. By relying on velocity information, we remove the need for specialized calibration targets while also avoiding the difficult problems of radar and cross-modal data association. We make the following contributions:

- we extend the work in [4] to enable full spatiotemporal calibration of monocular camera-3D radar pairs in arbitrary configurations;
- we prove that the calibration problem is identifiable and determine the motions that are required for reliable calibration;
- we analyze the accuracy of spatiotemporal calibration with varying amounts of sensor noise, through a simulation study;
- we carry out three different real-world experiments, which demonstrate that our algorithm is able to match the accuracy of an existing, target-based method and that we are able to perform calibration in different environments, including for sensors on board an AV.

In Section II, we survey existing extrinsic and spatiotemporal calibration algorithms for mm-wavelength radar sensors. Section III formulates spatiotemporal calibration as a batch, continuous-time estimation problem. We examine the identifiability of the calibration problem in Section IV. In Section V, we describe two simulation experiments designed to evaluate the robustness of our algorithm. In Section VI, we demonstrate the accuracy and flexibility of our algorithm by reporting on three real-world experiments in different environments. Finally, we summarize our contributions in Section VII.

## II. RELATED WORK

In this section, we survey spatial and spatiotemporal calibration algorithms that can be applied to mm-wavelength radars (as one of the sensors in a pair). Section II-A reviews algorithms for target-based extrinsic calibration, while Section II-B describes algorithms for target-free (or *targetless*) extrinsic calibration. In Section II-C, we discuss prior work on target-based spatiotemporal calibration.

### A. Target-Based Extrinsic Calibration

Early radar extrinsic calibration algorithms, developed prior to the widespread availability of 3D mm-wavelength radar units, focused on enabling 2D radar-camera data fusion. Many of these early extrinsic calibration techniques operate by computing the projective homography that maps points on the horizontal (sensing) radar plane to points on the camera image plane. Because radar sensors are inherently noisy, most calibration algorithms require specialized trihedral reflectors (see Fig. 8) that produce coincident, point-like ‘signals’ in both the radar and camera data, making the correspondence problem easier to solve [6]–[9]. Although 2D radar sensors are not able to properly measure the elevation of remote targets, they do nonetheless detect targets at a small elevation angle above the radar horizontal plane. Since the distance to off-plane targets will be slightly different, accurate calibration depends on ensuring that detected reflectors *do* lie on the radar horizontal plane. Sugimoto et al. [6] constrain the trihedral reflector position using the radar return signal strength. During calibration, the approach in [6] filters radar-camera measurement pairs by maximal return intensity.

More recent 2D radar extrinsic calibration algorithms often minimize a type of ‘reprojection error,’ that is, the error in the alignment of identifiable objects that appear within both sensors’ fields of view. Kim et al. [10] leverage reprojection error to estimate the radar-to-camera transform, but assume that radar measurements are strictly constrained to the zero-elevation plane. El Natour et al. [11] determine the radar-to-camera transform by intersecting backprojected camera rays with the 3D ‘arcs’ along which the 2D radar measurements must lie. Domhof et al. [12] use a specialized, structured calibration target that provides scale for the camera measurement, which enables extrinsic calibration through point cloud alignment. Peršić et al. [13] also perform extrinsic calibration via 3D point cloud alignment, but improve the overall accuracy by modelling the relationship between target return intensity and elevation angle. The ‘homography’ and ‘reprojection’ methods are summarized and compared by Oh et al. in [14], where the authors conclude that both have similar accuracy. Due to the infrastructure requirements (i.e., specialized targets), all of the methods above are restricted to sensor pairs that share overlapping fields of view. This requirement may be impossible to satisfy for certain sensor configurations. By leveraging constraints induced by the motion of rigidly-connected radar-camera pairs, we are able to calibrate sensors that do not share overlapping fields of view. Further, our approach does not require any specific infrastructure, enabling calibration under a wider range of conditions.

### B. Target-Free Extrinsic Calibration

Some extrinsic calibration algorithms do not require specialized retroreflective targets. Schöller et al. [15] train a neural network end-to-end to regress a rotation correction from raw camera images and radar data, for example. Peršić et al. [16] estimate the yaw angle (only) between radar, camera, and lidar sensors by aligning the trajectories of objects tracked by the sensors. These methods both require manual measurement of the translation parameters and also overlapping fields of view.

Heng [17] presents the first reprojection error-based 3D radar-lidar extrinsic calibration algorithm that does not require specialized targets or overlapping sensor fields of view. The approach in [17] estimates the extrinsic calibration between several lidar units and, using a known vehicle trajectory, constructs a 3D point cloud map. The radar-lidar extrinsic calibration parameters are then determined by minimizing two weighted residuals: the distance from the radar point measurements to the closest plane in the lidar map and the radial velocity error. This method requires the construction of a dense lidar map and known vehicle poses, however.

Instead of using feature positions, a subset of extrinsic calibration algorithms fuse ego-velocity and ego-motion measurements from the radar and second sensor, respectively. Since the motion of each sensor is estimated separately, these methods do not perform radar or cross-modal data association and are inherently ‘target-free.’ Kellner et al. [18] estimate the rotation between a car-mounted 2D radar and an IMU by minimizing the difference in estimated lateral velocities, expressed in the radar frame. While the radar ego-velocity measurements provide lateral velocity directly, determining the lateral velocity of the radar from IMU measurements requires the IMU angular velocity and accurate knowledge of the radar-IMU translation. Doer et al. [19] extend the approach in [18] to estimate the full extrinsic calibration for a 3D radar-IMU pair. Using simulated radar ego-velocity estimates corrupted by zero-mean Gaussian noise with a standard deviation of  $\Sigma = \text{diag}([0.018 \ 0.035 \ 0.102])$ , their method achieves a spatial calibration accuracy of 5 cm and  $5^\circ$ . Wise et al. [4] perform extrinsic calibration in continuous time using instantaneous radar ego-velocity measurements and camera egomotion measurements. Under a fixed temporal offset, the spatial calibration parameters estimated by this method are within 3 cm and  $1^\circ$ , per axis, of those determined by [2]. All of these techniques rely on ad-hoc temporal calibration schemes. Herein, we incorporate a principled temporal calibration method.

### C. Target-Based Spatiotemporal Calibration

To date, two radar spatiotemporal calibration algorithms have appeared in the literature, by Lee et al. [1] and by Peršić et al. [2]. The algorithm in [1] first calibrates the 2D radar-lidar spatial transform using the method of Peršić et al. [13]. As a second step, the lidar measurements are expressed in the radar reference frame and the azimuth error to distant targets is minimized to determine the temporal offset between the sensors. Peršić et al. [2] represent the trajectory of a target moving through the fields of view of multiple

sensors using a continuous-time Gaussian process model. This representation allows their algorithm to estimate the spatiotemporal calibration parameters by aligning the sensors’ trajectories. In general, jointly estimating all parameters as part of one maximum likelihood estimation problem yields superior accuracy [2], [20]. Notably, since both methods in [1] and [2] rely on known targets, they have the same limitations as the methods discussed in Section II-A.

## III. METHODOLOGY

We formulate radar-to-camera spatiotemporal calibration as a continuous-time batch estimation problem. In Section III-A, we describe the mathematical notation used throughout the paper. We choose to parameterize the smooth radar-camera trajectories using continuous-time B-splines; we review the properties of this representation in Section III-B. In Section III-C, we derive our radar and camera measurement models. With the necessary preliminaries in place, we then define the full estimation problem in Section III-D.

### A. Notation

Latin and Greek letters (e.g.,  $a$  and  $\alpha$ ) denote scalar variables, while boldface lower- and uppercase letters (e.g.,  $\mathbf{x}$  and  $\Theta$ ) denote vectors and matrices, respectively. A parenthesized superscript pair, for example,  $\mathbf{A}^{(i,j)}$ , indicates the  $i$ th row and the  $j$ th column of the matrix  $\mathbf{A}$ . A three-dimensional reference frame is designated by  $\underline{\mathcal{F}}$ . The translation vector from point  $a$  (often a reference frame origin) to  $b$ , expressed in  $\underline{\mathcal{F}}_a$ , is denoted by  $\mathbf{r}_a^{ba}$ . The translational velocity vector of point  $b$  relative to point  $a$ , expressed in  $\underline{\mathcal{F}}_a$ , is denoted by  $\mathbf{v}_a^{ba}$ . The angular velocity of frame  $\underline{\mathcal{F}}_a$  relative to a frame  $\underline{\mathcal{F}}_i$ , expressed in  $\underline{\mathcal{F}}_a$ , is denoted by  $\boldsymbol{\omega}_a^{ai}$ .

We denote rotation matrices by  $\mathbf{R}$ . For example,  $\mathbf{R}_{ab} \in \text{SO}(3)$  defines the rotation from  $\underline{\mathcal{F}}_b$  to  $\underline{\mathcal{F}}_a$ . We reserve  $\mathbf{T}$  for SE(3) transformation matrices. For example,  $\mathbf{T}_{ab}$  is the  $4 \times 4$  homogeneous matrix that defines the rigid-body transform from frame  $\underline{\mathcal{F}}_b$  to  $\underline{\mathcal{F}}_a$ . Our SE(3) matrix entries will generally be functions of time; we denote the transform from frame  $\underline{\mathcal{F}}_b$  to  $\underline{\mathcal{F}}_a$  at time  $t$  by

$$\mathbf{T}_{ab}(t) = \begin{bmatrix} \mathbf{R}_{ab}(t) & \mathbf{r}_a^{ba}(t) \\ \mathbf{0}^T & 1 \end{bmatrix}, \quad (1)$$

where  $\mathbf{R}_{ab}(t) \in \text{SO}(3)$  and  $\mathbf{r}_a^{ba}(t) \in \mathbb{R}^3$ . We use  $\mathbf{I}_n$  to denote the  $n$ -by- $n$  identity matrix.

The unary operator  $\wedge$  acts on  $\mathbf{r} \in \mathbb{R}^3$  to produce a skew-symmetric matrix such that  $\mathbf{r}^\wedge \mathbf{s}$  is equivalent to the cross product  $\mathbf{r} \times \mathbf{s}$ . The operators  $\exp(\cdot)$  and  $\log(\cdot)$  map from the Lie algebra  $\mathfrak{so}(3)$  to the Lie group  $\text{SO}(3)$  and vice versa, respectively [21].

### B. Continuous-Time Trajectory Representation

Temporal calibration is most easily formulated as a continuous-time problem, in part because the batch optimization procedure incrementally time-shifts the measurements from one sensor. In turn, we require the ability to query the pose of the radar or the camera at arbitrary points in time.

To enable this, we parameterize the trajectory of the radar-camera pair using the B-spline representation from Sommer et al. [22]. This representation is briefly reviewed below. We refer readers to Sommer et al. [22], de Boor [23], and Qin [24] for additional details.

A B-spline of order  $k$  is a function of one continuous parameter (e.g., time) and a finite set of control points; for brevity, we restrict our example here to control points  $\{\mathbf{p}_0, \dots, \mathbf{p}_N \mid \mathbf{p}_i \in \mathbb{R}^d\}$ . In a uniformly-spaced B-spline, each control point is assigned a time (or *knot*)  $t_i = t_0 + i\Delta t$ , where  $t_0$  marks the beginning of the spline and  $\Delta t$  is the time between knots. Evaluating a  $k^{\text{th}}$  order B-spline at time  $t$ , where  $t_i \leq t < t_{i+1}$ , requires the set of  $k$  control points over the knot sequence  $t_i, \dots, t_{i+k-1}$ . As a result, the end point of a B-spline of length  $N$  and order  $k$  is at time  $t_{N-k+1}$ .

The first step in computing the value of a  $k^{\text{th}}$  order B-spline at time  $t$  is to convert  $t$  to the ‘normalized’ time  $u = \frac{t-t_i}{t_{i+1}-t_i}$ . Given  $u$ , the value of the  $k^{\text{th}}$  order B-spline is defined as

$$\mathbf{p}(u) = [\mathbf{p}_i \quad \mathbf{d}_1^i \quad \dots \quad \mathbf{d}_{k-1}^i] \tilde{\mathbf{M}}_k \mathbf{u}, \quad (2)$$

where  $\mathbf{u}^T = [1 \ u \ u^2 \ \dots \ u^{k-1}]$  and  $\mathbf{d}_j^i = \mathbf{p}_{i+j} - \mathbf{p}_{i+j-1}$ . The elements of the  $k \times k$  mixing matrix,  $\tilde{\mathbf{M}}_k$ , are defined by,

$$\tilde{\mathbf{M}}_k^{(a,n)} = \sum_{s=a}^{k-1} m_k^{(s,n)}, \quad (3)$$

$$m_k^{(s,n)} = \frac{C_{k-1}^n}{(k-1)!} \sum_{l=s}^{k-1} (-1)^{l-s} C_k^{l-s} (k-1-l)^{k-1-n} \quad (4)$$

$$a, s, n \in \{0, \dots, k-1\},$$

where scalar  $C_j^i = \frac{j!}{i!(j-i)!}$ . Substituting  $\lambda(u) = \tilde{\mathbf{M}}_k \mathbf{u}$  into Equation (2) results in

$$\mathbf{p}(u) = \mathbf{p}_i + \sum_{j=1}^{k-1} \lambda_j(u) \mathbf{d}_j^i. \quad (5)$$

Equation (5) can describe the smooth translation of a rigid-body in continuous time (see Figure 10 in Section VI for an example).

While our development above focuses on vector space splines, B-splines can also be defined on Lie groups, including the group  $\text{SO}(3)$  of rotations,

$$\mathbf{R}(u) = \mathbf{R}_i \prod_{j=1}^{k-1} \exp(\lambda_j(u) \phi_j^i), \quad (6)$$

where  $\mathbf{R}_i$  is a control point of the rotation spline and  $\phi_j^i = \log(\mathbf{R}_{i+j-1}^T \mathbf{R}_{i+j})$ . We use two B-splines, one on  $\text{SO}(3)$  and one on  $\mathbb{R}^3$ , as our complete continuous-time representation of the radar-camera trajectory.

### C. Sensor Measurement Models

In order to perform spatiotemporal calibration, we require a measurement model for the radar unit. Radars emit electromagnetic (EM) waves that reflect off of surfaces in the environment. By receiving and processing reflected waves, a radar unit measures the range, azimuth, elevation, range-rate

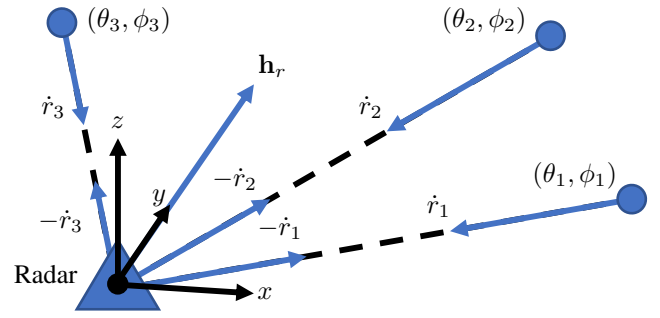


Fig. 2: Illustration of our radar measurement model. The radar EM wave reflects off of three (or more) non-collinear, stationary landmarks in the environment, yielding azimuth, elevation, and range-rate measurements to each landmark. Using these data, we estimate the radar velocity relative to the world reference frame, expressed in the radar reference frame.

(the radial velocity of a target), and radar-cross section (reflectivity) of a target. Due to the relatively long EM wavelength used by radars, the reflected ‘‘location’’ of an EM wave from a target can vary based on the relative orientation between the radar and the target [3]. Additionally, multipath reflections can occur when the wave bounces off of multiple surfaces before returning to the radar receiver, which can bias measurements of targets and introduce false detections [3].

For each received reflection  $l$  from an environmental feature (i.e., an object that we identify as a *landmark*), the radar measures the range  $r_l$ , azimuth  $\theta_l$ , elevation  $\phi_l$ , and range-rate  $\dot{r}_l$ . We assume that the observed landmarks are stationary with respect to a world frame,  $\mathcal{F}_w$ ; measurements are resolved in the radar reference frame,  $\mathcal{F}_r$ . The range-rate measurement is the dot product between the velocity of the radar unit itself,  $\mathbf{h}_r \in \mathbb{R}^3$ , and the unit vector  $\hat{\mathbf{r}}_l \in \mathbb{S}^2$  defined by  $\theta_l$  and  $\phi_l$ . Given radar measurements to three (or more) non-collinear, stationary landmarks, the unit direction vectors and their associated range-rates can be used to reconstruct the radar velocity  $\mathbf{h}_r$ , as shown in Figure 2.

Stahoviak [5] and Doer et al. [25] demonstrate that, given  $N > 3$  stationary landmarks, one can estimate the ego-velocity of the radar by solving the over-constrained linear least-squares problem

$$\mathbf{h}_r^* = \min_{\mathbf{h}_r} \mathbf{e}_{ego}^T \mathbf{e}_{ego}, \quad (7)$$

where

$$\mathbf{e}_{ego} = \mathbf{H} \mathbf{x} - \mathbf{y} = \begin{bmatrix} \hat{\mathbf{r}}_0^T \\ \vdots \\ \hat{\mathbf{r}}_N^T \end{bmatrix} \mathbf{h}_r - \begin{bmatrix} \dot{r}_0 \\ \vdots \\ \dot{r}_N \end{bmatrix} \quad (8)$$

Equation (8) has its specific form because we wish to estimate the velocity of the radar with respect to the static world frame, and not vice versa. The estimated ego-velocity covariance is

$$\Sigma_v = \frac{(\mathbf{e}_{ego}^T \mathbf{e}_{ego})(\mathbf{H}^T \mathbf{H})}{N-3}. \quad (9)$$

We use RANSAC [5], [25] and radar cross-section thresholding to remove outliers. The two main sources of outliers are targets that move relative to the inertial reference frame and spurious multipath reflections. Empirically, RANSAC elimi-



nates outliers from these two sources if the range-rate biases are sufficiently large. However, there are two subtle cases where the measurement bias from multipath reflections may be relatively small. In the first case, the difference between the transmission and return angles is small. In the second case, the transmission and return angles are symmetric about the radar ego-velocity direction (see Section 8.9 in [3]). The returns from these multipath reflections have a low radar cross-section and are rejected by radar cross-section thresholding.

Given our B-Spline trajectory representation, the measurement model for the radar ego-velocity (at time  $t_j$ )

$$\begin{aligned} \mathbf{h}_{r_j} &= -\dot{\mathbf{r}}_r^{wr}(t_j + \tau) - \boldsymbol{\omega}_r^{rw}(t_j + \tau) \wedge \mathbf{r}_r^{wr}(t_j + \tau) \\ &\quad + \mathbf{n}_{v_j}, \\ \mathbf{n}_{v_j} &\sim \mathcal{N}(\mathbf{0}_{3 \times 1}, \boldsymbol{\Sigma}_{v_j}), \end{aligned} \quad (10)$$

where  $\tau$  is the temporal offset of the radar measurements relative to the camera measurements and  $\mathbf{n}_{v_j}$  is the radar velocity measurement noise term that we assume is a zero-mean Gaussian with covariance matrix  $\boldsymbol{\Sigma}_{v_j}$  (see Equation (9)). From the radar ego-velocity model, the error residual is

$$\begin{aligned} \mathbf{e}_{v_j} &= \mathbf{h}_{r_j} + \dot{\mathbf{r}}_r^{wr}(t_j + \tau) + \\ &\quad \boldsymbol{\omega}_r^{rw}(t_j + \tau) \wedge \mathbf{r}_r^{wr}(t_j + \tau) - \mathbf{n}_{v_j}. \end{aligned} \quad (11)$$

To estimate the ego-motion of the camera, we use a monocular SLAM algorithm that operates independently of the radar. By observing fixed landmarks in the environment, monocular SLAM is capable of determining the transformation between the camera reference frame,  $\mathcal{F}_c$ , and the world frame,  $\mathcal{F}_w$ , up to an unknown scale factor  $\alpha$  [26]. Our (scaled) camera pose measurement model is given by

$$\begin{aligned} \mathbf{R}_{cw,t_k} &= \exp(\mathbf{n}_{r,k}) \mathbf{R}_{cr} \mathbf{R}_{wr}(t_k)^T, \\ \mathbf{n}_{r,k} &\sim \mathcal{N}(\mathbf{0}_{3 \times 1}, \boldsymbol{\Sigma}_r), \end{aligned} \quad (12)$$

$$\begin{aligned} \mathbf{r}_{c,t_k}^{wc} &= \alpha (\mathbf{R}_{cr} \mathbf{r}_r^{wr}(t_k) + \mathbf{r}_c^{rc}) + \mathbf{n}_{t,k}, \\ \mathbf{n}_{t,k} &\sim \mathcal{N}(\mathbf{0}_{3 \times 1}, \boldsymbol{\Sigma}_t), \end{aligned} \quad (13)$$

where  $\mathbf{n}_{r,k}$  and  $\mathbf{n}_{t,k}$  are zero-mean Gaussian noise terms for the camera rotation and translation measurements, respectively, with covariances matrices  $\boldsymbol{\Sigma}_r$  and  $\boldsymbol{\Sigma}_t$ . The resulting error equations are

$$\mathbf{e}_{r,t_k} = \log(\mathbf{R}_{cw,t_k} \mathbf{R}_{wr}(t_k) \mathbf{R}_{cr}^T), \quad (14)$$

$$\mathbf{e}_{t,t_k} = \mathbf{r}_{c,t_k}^{wc} - \alpha (\mathbf{R}_{cr} \mathbf{r}_r^{wr}(t_k) + \mathbf{r}_c^{rc}) - \mathbf{n}_{t,k}. \quad (15)$$

We note that a monocular visual odometry (VO) algorithm (i.e., localization without loop closure) could provide camera ego-motion measurements, but visual drift will bias these measurements and decrease calibration accuracy. Additionally, given a radar-camera system with unknown spatial calibration parameters and temporal offset, correlating the radar ego-velocity with the visual features of the camera is unlikely to minimize pose drift. As a result, we use the coupling of the radar ego-velocities, camera poses, and spatial calibration parameters to perform spatiotemporal calibration. However, the radar ego-velocity is a local property of a trajectory and does not mitigate pose errors induced by visual drift.

#### D. The Spatiotemporal Calibration Problem

The set of parameters  $\mathbf{x}$  that we wish to estimate are the spline control points ( $\mathbf{r}_{0..N} \in \mathbb{R}^3$ ,  $\mathbf{R}_{0..N} \in SO(3)$ ), the extrinsic calibration parameters ( $\mathbf{R}_{cr}, \mathbf{r}_c^{rc}$ ), the camera translation scale factor ( $\alpha$ ), and the temporal offset ( $\tau$ ),

$$\mathbf{x} = \{ \mathbf{r}_0, \dots, \mathbf{r}_N, \mathbf{R}_0, \dots, \mathbf{R}_N, \mathbf{R}_{cr}, \mathbf{r}_c^{rc}, \alpha, \tau \}. \quad (16)$$

Given  $N_r$  radar measurements and  $N_c$  camera measurements, we minimize the following cost function,

$$\begin{aligned} \mathbf{x}^* &= \min_{\mathbf{x}} \sum_{j=1}^{N_r} \mathbf{e}_{v_j}^T \boldsymbol{\Sigma}_{v_j}^{-1} \mathbf{e}_{v_j} + \\ &\quad \sum_{k=1}^{N_c} \mathbf{e}_{r,t_k}^T \boldsymbol{\Sigma}_r^{-1} \mathbf{e}_{r,t_k} + \mathbf{e}_{t,t_k}^T \boldsymbol{\Sigma}_t^{-1} \mathbf{e}_{t,t_k}. \end{aligned} \quad (17)$$

We perform this minimization using the Ceres solver, a standard non-linear least squares solver [27]. The ability to calibrate all of the relevant parameters depends upon the identifiability of problem, which we discuss in the next section.

#### IV. IDENTIFIABILITY

In this section, we show that the calibration problem is identifiable given sufficient excitation of the radar-camera system. Our approach is to determine the observability, or ‘instantaneous identifiability,’ of the system at several different points in time, assuming that the system follows a varying trajectory. We consider local identifiability (cf. locally weak observability) along a trajectory segment in Section IV-B, after introducing the requisite observability rank condition in Section IV-A. A similar approach has been taken in [28] and [29] and elsewhere. In Section A-C, we describe several ‘degenerate’ motions for which the identifiability condition does not hold. We leave the complete characterization of the sets of unidentifiable trajectories as future work.

##### A. The Observability Rank Condition

We make use of the criterion from Hermann and Krener [30] as part of our identifiability analysis. A system  $S$ , written in control-affine form as

$$S \begin{cases} \dot{\mathbf{x}} = \mathbf{f}_0(\mathbf{x}) + \sum_{j=1}^p \mathbf{f}_j(\mathbf{x}) u_j \\ \mathbf{y} = \mathbf{h}(\mathbf{x}) \end{cases}, \quad (18)$$

with the drift vector field  $\mathbf{f}_0(\mathbf{x})$  and control inputs  $u_j$  (for  $j = 1, \dots, p$ ), is locally weakly observable if the matrix  $\mathbf{O}$  of the gradients of the Lie derivatives with respect to the system state has full column rank.

The Lie derivative, or directional derivative, of a smooth scalar function  $h$  with respect to the smooth vector field  $\mathbf{f}$  at the point  $\mathbf{x}$  is

$$L_{\mathbf{f}} h(\mathbf{x}) = \nabla_{\mathbf{f}} h(\mathbf{x}) = \frac{\partial h(\mathbf{x})}{\partial \mathbf{x}} \mathbf{f}(\mathbf{x}). \quad (19)$$

The  $n^{\text{th}}$  Lie derivative of  $h$  with respect to  $\mathbf{x}$  along  $\mathbf{f}$  is defined recursively as

$$L_{\mathbf{f}}^n h(\mathbf{x}) = \frac{\partial L_{\mathbf{f}}^{n-1} h(\mathbf{x})}{\partial \mathbf{x}} \mathbf{f}(\mathbf{x}), \quad (20)$$

where  $L^0 h(\mathbf{x}) = h(\mathbf{x})$ . We note that the matrix  $\mathbf{O}$  has, potentially, an infinite number of rows, but it is sufficient to show that a finite number of rows yield a matrix of full column rank.

### B. Identifiability of Radar-Camera Calibration

We begin by simplifying the state (and parameter) vector that we aim to estimate. We are able to measure the camera pose up to scale [26] and the radar velocity in the radar frame [5]. Since we are working in continuous time (or, roughly equivalently, if there are a sufficient number of closely-spaced radar and camera measurements), then the scaled velocity of the camera in the camera reference frame  $\alpha \mathbf{v}_c^{cw}(t_i)$ , the rotational velocity of the camera  $\boldsymbol{\omega}_c(t_i)$  in the camera frame, the radar velocity  $\mathbf{v}_r^{rw}(t_i + \tau)$  in the radar frame, and the time derivative of the radar velocity  $\dot{\mathbf{v}}(t_i + \tau)$  in the radar frame are all available. For the purposes of identifiability, we are able to define the following, modified measurement model,

$$\mathbf{h}(t_i) = \alpha(\mathbf{R}_{cr} \mathbf{v}_r^{rw}(t_i + \tau) - \boldsymbol{\omega}_c(t_i) \wedge \mathbf{r}_c^{rc}), \quad (21)$$

where  $\mathbf{h}(t_i)$  is the scaled linear velocity of the camera ( $\mathbf{v}_c^{cw}$ ) and  $\boldsymbol{\omega}_c$  is the angular velocity of the camera, both relative to the camera frame. This modified measurement model does not directly rely on the pose of the radar, thus simplifying the set of parameters that we wish to determine to

$$\tilde{\mathbf{x}} = \{\mathbf{r}_c^{rc}, \mathbf{R}_{cr}, \alpha, \tau\}. \quad (22)$$

To decrease the notational burden, we drop the superscripts and subscripts defining the velocities and extrinsic transform parameters. The gradient of the zeroth-order Lie derivative of the  $i$ th measurement is

$$\nabla_{\tilde{\mathbf{x}}} L_0 \mathbf{h}(t_i) = \begin{bmatrix} -\alpha \boldsymbol{\omega}(t_i) \wedge & -\alpha(\mathbf{R} \mathbf{v}(t_i + \tau)) \wedge \mathbf{J} \\ \mathbf{R} \mathbf{v}(t_i + \tau) - \boldsymbol{\omega}(t_i) \wedge \mathbf{r} & \alpha \mathbf{R} \dot{\mathbf{v}}(t_i + \tau) \end{bmatrix}, \quad (23)$$

where  $\mathbf{J}$  is the Lie algebra left Jacobian of  $\mathbf{R}_{cr}$  [21]. Since the parameters of interest are constant with respect to time, we are able to stack the gradients of several Lie derivatives (at different points in time) to form the observability matrix,

$$\mathbf{O} = \begin{bmatrix} \nabla_{\tilde{\mathbf{x}}} L_0 \mathbf{h}(t_1) \\ \nabla_{\tilde{\mathbf{x}}} L_0 \mathbf{h}(t_2) \\ \nabla_{\tilde{\mathbf{x}}} L_0 \mathbf{h}(t_3) \end{bmatrix}, \quad (24)$$

which, using block Gaussian elimination, can be shown to have full column rank when three or more sets of measurements are available.<sup>1</sup>

Two comments regarding the analysis are in order. First, we note that the analysis is simplified by considering the modified measurement equation only (without any higher-order Lie derivatives). Second, there is a subtlety involved in stacking the gradients of the Lie derivatives at different points in time. The modified measurement equation depends upon the time derivatives of the camera pose and the radar ego-velocity—this implies that, although we do not consider specific control inputs, the system dynamics must be non-null. Stated differently, varied motion of the radar-camera pair is

necessary to ensure identifiability; we discuss this requirement further in the next section. Also, it is worth noting that the observation times must span the temporal offset period [31].

### C. Degenerate Motions

There are motions that cause the matrix  $\mathbf{O}$  in Equation (41) to lose full column rank. First, this system relies on linear and rotational velocities and accelerations, so the matrix will lose full column rank when the system is stationary with respect to the world frame or moving with constant linear or angular velocity. Second, in Wise et al. [4], we showed that the system must undergo rotation about two nonparallel axes in order for the observability matrix to be full rank. This requirement also applies to the present analysis. To show this, we can align the angular velocity and angular acceleration vectors by substituting  $\boldsymbol{\alpha}_c^{ci} = \eta \boldsymbol{\omega}_c^{cw}$ , where  $\eta$  is an arbitrary constant, into Equation (41). This substitution is equivalent to asserting that the system rotates about one axis only, resulting in an observability matrix that is rank-deficient.

## V. SIMULATION STUDIES

In order to test the robustness of our algorithm to measurement noise, we carried out a series of simulation studies. We generated a pair of 100 simulated camera-radar datasets using two different trajectories and varying noise levels (see Figures 3 and 4). The nominal (noise-free) trajectories were selected to ensure sufficient excitation of the camera-radar pair. The median linear and rotational velocities for the trajectory shown in Figure 3 were, respectively, higher and lower than the velocities of the trajectory shown in Figure 4. The pair of trajectories were constructed by integrating their linear and rotational accelerations.

After constructing the trajectories, we computed the radar ego-velocity and camera pose measurements. Since radar measurements are antenna configuration and environment specific, these measurements were not generated at the electromagnetic propagation level. Simulated radar ego-velocity measurements (i.e.,  $\mathbf{h}_{r_k}$ ) were computed using the known linear and rotational velocities defined by the trajectory. Consequently, our simulated radar measurements generalize to any radar and environment that produce an unbiased 3D ego-velocity estimate. Simulated camera pose measurements (i.e.,  $\mathbf{R}_{cw, t_k}$  and  $\mathbf{t}_{c, t_k}^{wc}$ ) were derived from observations of a series of landmark points, arranged in a 2D grid. This configuration of points matches the configuration of a standard ‘checkerboard’ camera calibration target. In the targetless setting, we can only estimate the position of the camera up to an unknown scale [26], so the checkerboard tracking algorithm is given an incorrect size for the checkerboard squares.

For each simulation, we added zero-mean Gaussian noise to the radar ego-velocity measurements ( $\boldsymbol{\Sigma}_{v_j} = \sigma_r^2 \mathbf{I}_{3 \times 3}$ ) and to the camera measurements of the checkerboard corners on the simulated image plane ( $\boldsymbol{\Sigma}_{p_k} = \sigma_c^2 \mathbf{I}_{2 \times 2}$ ). For our experiments, we adjusted the radar ego-velocity variance ( $\sigma_r$ ) between 0.05 m/s and 0.15 m/s. Based on our real-world experiments (see Section VI), we have found that the radar ego-velocity measurement noise is closer to the lower end of this range,

<sup>1</sup>We omit the full derivation for brevity, and note that the rank condition can be verified in this case using any symbolic algebra package.

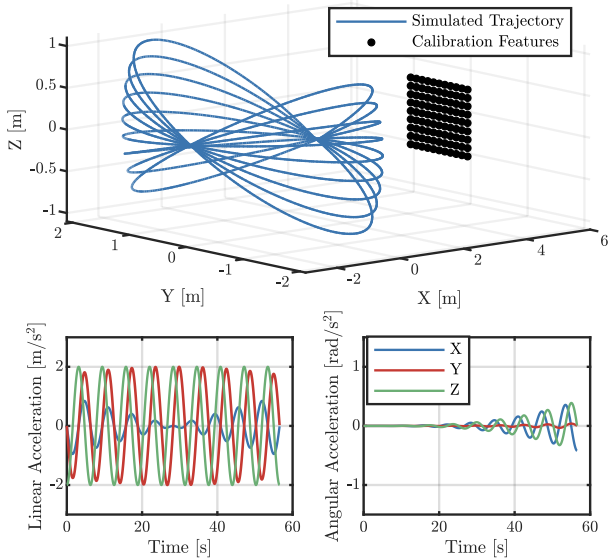


Fig. 3: High linear and low rotational velocity trajectory for the simulated experiments with associated linear and angular acceleration plots.

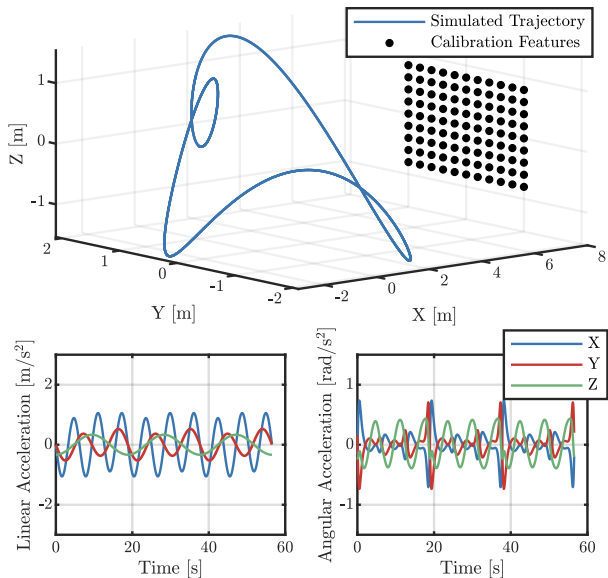


Fig. 4: Low linear and high rotational velocity trajectory for the simulated experiments with associated linear and angular acceleration plots.

unless the environment is sparse and too few valid radar returns are captured. We adjusted the variance of the noise added to the measured checkerboard corner coordinates ( $\sigma_c$ ) between 0.1 and 0.4 pixels; these noise levels are similar to the observed noise in our real-world experiments [4].

The error distributions for the spatial calibration parameter estimates ( $\mathbf{R}_{cr}$ ,  $\mathbf{r}_c^{Tc}$ ), scale factor ( $\alpha$ ), and temporal offset ( $\tau$ ) are shown in Figures 5 and 6, across the 100 simulation trials. For the high linear and low rotational velocity trajectory, even in the high-noise regime, the error in the rotation and scale estimates remains at less than two degrees and one percent, respectively. However, high levels of noise in the radar ego-velocity measurements result in substantially larger (and

more widely distributed) errors in the estimate of the relative translation of the sensors and of the temporal offset; the errors can be as large as 15 cm and 30 ms, respectively. This sensitivity indicates that, prior to use in our algorithm, the radar data should be filtered to remove high-noise measurements whenever possible.

If the system follows the high-velocity trajectory in Figure 4, then radar data filtering may not be necessary. As shown in Figure 6, calibrating the radar along this trajectory results in similar scale and rotation estimation accuracy as the low velocity trajectory, but drastically improves the translation and temporal offset estimates; the errors are within 10 cm and 10 ms, respectively. Additionally, our algorithm achieves a comparable spatial calibration error to Doer et al. [19] on noisier radar ego-velocity data. However, this high rotational velocity trajectory is challenging for real-world camera localization and is not necessary if the radar data are sufficiently accurate.

## VI. REAL-WORLD EXPERIMENTS

To verify the performance and accuracy of our algorithm, we carried out a series of real-world experiments involving three different radar-camera systems. We discuss the various systems and their implementation details in Section VI-A. In Section VI-B, we show that the set of spatiotemporal calibration parameters estimated by our algorithm have a similar level of alignment accuracy as the parameters estimated by the target-based method of Peršić et al. [2]. In Section VI-C, we demonstrate how spatiotemporal calibration can improve the performance of camera-radar-IMU odometry. Finally, in Section VI-D, we evaluate the accuracy of our algorithm in a challenging situation involving sensors mounted on an autonomous vehicle.

### A. Data Collection and Data Preprocessing

The data collection systems are different for each experiment, however each system consists of at least one radar and one camera. The system discussed in Section VI-B is a handheld sensor rig that incorporates a Texas Instruments (TI) AWR1843BOOST radar and Point Grey Flea3 camera. The measurement update rates for the sensors are 20 Hz and 30 Hz, respectively. For the experiments in Section VI-C, the data are from the IRS Radar Thermal Visual Inertial dataset that is publicly-available [32]. The data collection system [32] is a handheld rig that mounts on a drone, where measurements are acquired from a Texas Instruments IWR6843AOP unit, an IDS UI-3241 camera, and an Analog Devices ADIS16448 inertial measurement unit (IMU), operating at frequencies of 10 Hz, 20 Hz, and 409 Hz, respectively. Doer et al. [32] provides additional details about this system. In Section VI-D, the data collection system [33] incorporates a vehicle-mounted TI AWR1843BOOST radar and three Point Grey Flea3 GigE cameras operating at frequencies of 25 Hz and 16 Hz, respectively.

In our real-world experiments, we use two similar radars that primarily differ in angular resolutions. If two targets have an identical range and range-rate, and are separated by less than the angular resolution, then the targets will blend together

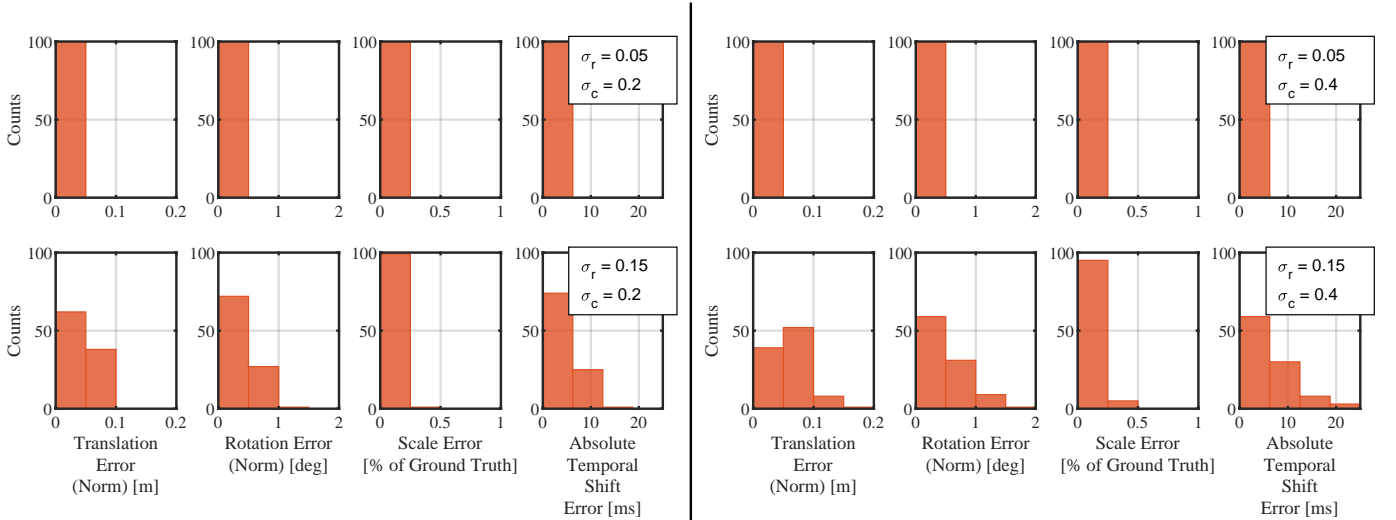


Fig. 5: High linear and low rotational velocity trajectory spatiotemporal calibration results from the simulated experiments. Each subplot is a histogram of the error between the estimated and true parameter values for 100 experiments at a given level of measurement noise. Each row presents the results for a level of measurement noise. The levels of measurement noise are a combination of two radar measurement noise levels ( $\sigma_r = 0.05$  or  $0.2$  m/s) and two camera pixel measurement noise levels ( $\sigma_c = 0.1$  or  $0.4$  pixels). The columns are the error distribution plots for a calibration parameter.

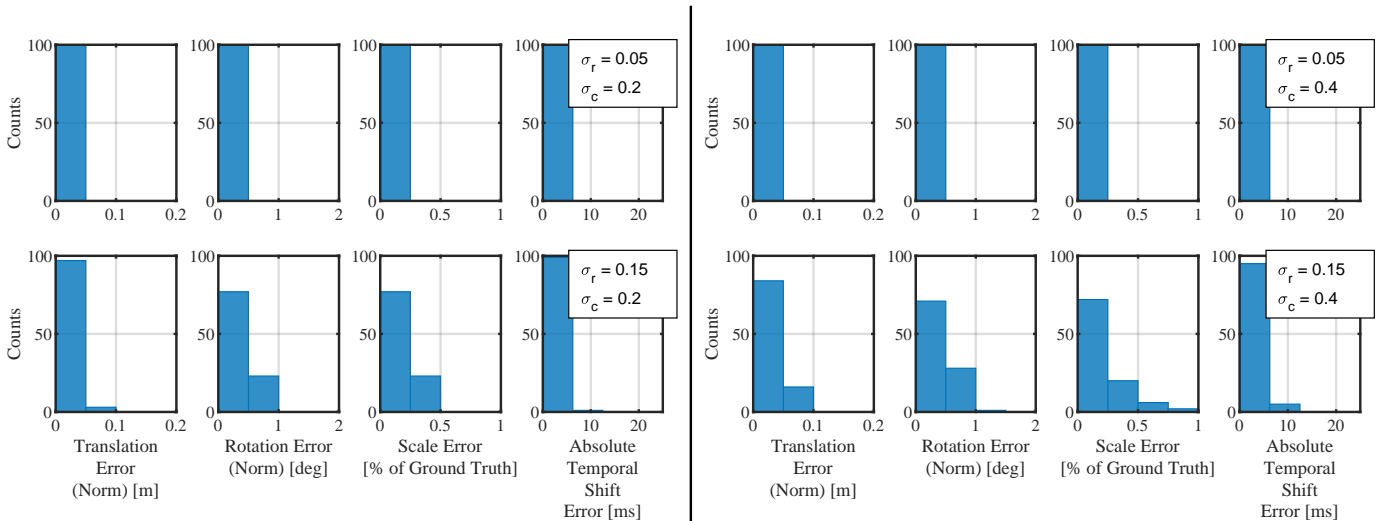


Fig. 6: Low linear and high rotational velocity trajectory spatiotemporal calibration results from the simulated experiments. Each subplot is a histogram of the error between the estimated and true parameter values for 100 experiments at a given level of measurement noise. Each row presents the results for a level of measurement noise. The levels of measurement noise are a combination of two radar measurement noise levels ( $\sigma_r = 0.05$  or  $0.2$  m/s) and two camera pixel measurement noise levels ( $\sigma_c = 0.1$  or  $0.4$  pixels). The columns are the error distribution plots for a calibration parameter.

which biases the radar measurement. The AWR1843BOOST has azimuth and elevation resolutions of  $15^\circ$  and  $58^\circ$ , respectively, while the IWR6843AOP has azimuth and elevation resolutions of  $30^\circ$ . As we show in Sections VI-B, VI-C, and VI-D, our algorithm is capable of calibrating both radars even though they have differing radar resolutions. For additional information on the radars used in our experiments, we refer the reader to the AWR1843BOOST and IWR6843AOP user manuals [34], [35].

To ensure accurate ego-velocity estimation for our experiments, we set the maximum measurable range-rate and constant false alarm rate (CFAR) thresholds for our radar units.

The maximum range-rate of the radar must be set above the maximum velocity of the data collection platform because the ego-velocity estimates will saturate at this value. However, an inverse relationship exists between the maximum range-rate and maximum range settings and these must be properly balanced for the operating environment [3]. The on-board radar pre-processing pipeline incorporates a CFAR detector that differentiates targets from background noise in the received EM signal [3]. Since the definition of background noise is also environment-dependant, we set the CFAR threshold to ensure that the ego-velocity estimator returned a sufficient number of inliers, while minimizing the number of outliers.



Before each experiment, we performed a series of ‘test’ data collection runs to tune these settings, ensuring that the ego-velocity estimates were not saturating, that there were at least 15 inliers for each measurement, and that the inlier to outlier ratio was above 50%.

There are three data preprocessing steps for the experiments discussed in Sections VI-B and VI-C, while the experiment in Section VI-D requires a fourth additional preprocessing step. Prior to estimating the calibration parameters using our algorithm, we first determine radar ego-velocity estimates using the algorithm from [25].<sup>2</sup> Second, we rectify the camera images to remove lens distortion effects. Third, we use the feature-based, monocular simultaneous localization and mapping (SLAM) algorithm ORB-SLAM3 [36] to provide an initial estimate of the (arbitrarily-scaled) pose of the camera at the time of each image acquisition. While camera pose estimation is possible with any monocular SLAM, we chose this package for its robustness and accuracy [36]. Finally, for the experiment in Section VI-D, we remove outlier radar ego-velocity and camera pose estimates using a median filter. The median filter computes the local median and standard deviation of the signals across a window of time—200 ms and 850 ms for the radar and camera, respectively. If the measurement at the center of the window is greater than a chosen threshold from the median, the measurement is treated as an outlier. For the tests in Section VI-D, the threshold is set to three standard deviations from the median, since this value eliminates gross outliers without removing noisy, but valid, portions of the signals. We found that this step was necessary to ensure data integrity.

### B. Handheld Rig Experiment

In this experiment, we compared the calibration parameters estimated by our algorithm against the parameters determined by the target-based method in Peršić et al. [2]. To compare the two approaches, we used a handheld rig to collect a dataset consisting of two parts: one part with no visible calibration targets (for our algorithm) and one part with visible targets for target-based calibration. We collected both parts on the dataset during one continuous run, without power-cycling the sensors. Our quality metric in this case is based on the results from target-based calibration (which can be treated as the ‘gold standard,’ effectively).

We used the first part of the dataset to perform targetless radar-camera calibration with our algorithm. The procedure consisted of moving the sensor rig, shown in Figure 7, throughout the office environment shown in Figure 9. A segment of the system trajectory estimated by our algorithm is plotted in Figure 10. Then, we used the second part of the dataset to perform target-based calibration with the algorithm described in Peršić et al. [2]. In this case, the procedure consisted of moving a trihedral retroreflective target, shown in Figure 8, in front of the stationary radar-camera rig. The second part of the dataset was also used to evaluate the relative accuracy of the parameters estimated by both algorithms.

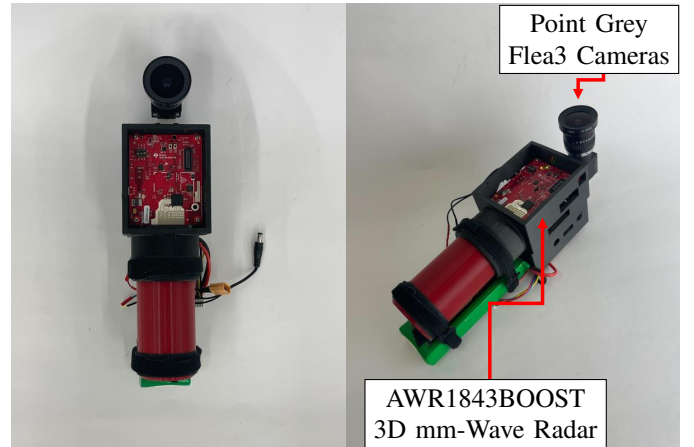


Fig. 7: Two pictures of our handheld data collection rig. The left image is a front view and the right image is an isometric view of the radar-camera unit. The radar antennas are mounted in the white area on the red circuit board. From our CAD model of the handheld rig, the radar-camera translation parameters (i.e., the components of  $\mathbf{r}_c^{r_c}$ ) are  $r_x = 0.1$ ,  $r_y = 10.5$ , and  $r_z = -1.0$  cm.

Our trihedral retroreflective target is specially-constructed for calibration evaluation, and consists of a trihedral radar retroreflective ‘corner’ and a visual AprilTag [37] pattern printed on paper. The target, shown in Figure 8, has the AprilTag (which is EM transparent) mounted in front of the retroreflector. Using the known AprilTag scale, the pose of the camera relative to the AprilTag reference frame can be established. The distance from the origin of the AprilTag frame to the corner of the retroreflector is also known. During data collection, we kept the reflector opening pointed at the radar to ensure a consistent radar reflection.

We quantify the calibration accuracy based on a ‘reprojection error’ metric. The reprojection error is the distance between the position of the retroreflector corner predicted from the camera observations and the position measured by the radar, expressed in the radar frame. The retroreflector is more consistently detected than the AprilTag, and so we linearly interpolate the measured position of the trihedral retroreflector corner by the radar at the image timestamps.

Overall, our algorithm achieves results that are comparable to the method from Peršić et al. [2]. Table I shows that the estimated translation and rotation, are, per axis, within 1.6 cm and 3 degrees, respectively, of the values estimated by the target-based method, which is expected from the fixed temporal offset case in Wise et al. [4]. Additionally, our estimated temporal offset differs from the target-based method by only 6 ms. Figure 11 shows that our algorithm, in a completely targetless manner, produces a reprojection error distribution with a median that is only 3 mm larger than the target-based method.

### C. IRS Radar Thermal Visual Inertial Datasets

In this section, we demonstrate the versatility of our algorithm by making use of our estimated calibration parameters to improve the accuracy of camera-radar-IMU odometry for the system described by Doer and Trommer [32]. The extrinsic

<sup>2</sup>Available at: <https://github.com/christopherdoer/reve>

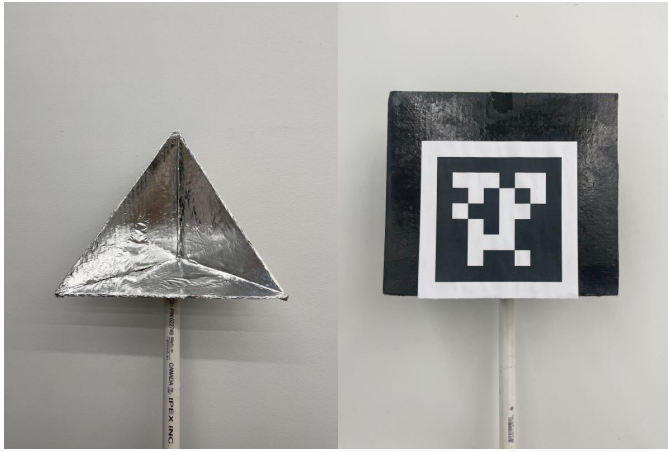


Fig. 8: Our specialized retroreflective radar target used for verification. The left image shows the retroreflector alone, while the right image shows an AprilTag mounted to a flat cardboard backing that is attached to the front of the retroreflector. The cardboard material is fully transparent to the radar EM wave.

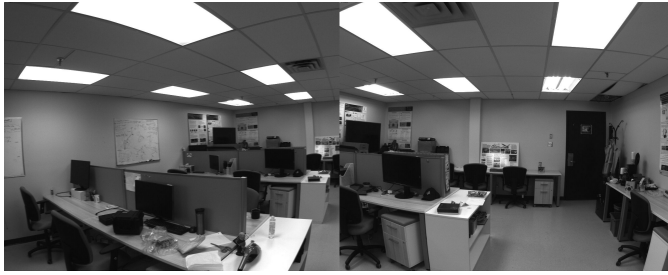


Fig. 9: Images from our handheld sensor rig calibration dataset, showing two views of the feature-rich indoor test environment.

calibration parameters that accompany the IRS dataset were determined using the radar-IMU extrinsic calibration process described in [19] with ad-hoc temporal calibration. Post-hoc calibration of the radar and camera for the IRS is challenging because the test environments do not contain any trihedral reflectors (thus, target-based spatiotemporal calibration is not possible) and the motion of the sensor platform is constrained (i.e., there are no deliberate excitations for calibration). To the best of the authors’ knowledge, our approach is the only technique that can estimate all of the spatiotemporal calibration parameters for the datasets described in Doer and Trommer [32].

We chose to calibrate, and to evaluate the calibration quality, for three IRS datasets from the total of nine available datasets. We calibrated using the Gym, MoCap Easy, and MoCap Medium datasets. These datasets were collected in two environments with varying numbers of features: a large, sparse

TABLE I: Calibration parameters for our handheld dataset. The values in each row are estimated by a different algorithm. The rotation between the sensors is given in roll-pitch-yaw (i.e.,  $\theta_x, \theta_y, \theta_z$ ) Euler angle form.

	$r_x$ [cm]	$r_y$ [cm]	$r_z$ [cm]	$\theta_x$ [rads]	$\theta_y$ [rads]	$\theta_z$ [rads]	$\tau$ [ms]
Peršić [2]	-1.60	11.9	-5.02	-1.59	0.07	-3.12	-63.8
Ours	-0.48	12.2	-3.42	-1.62	0.02	-3.15	-57.9

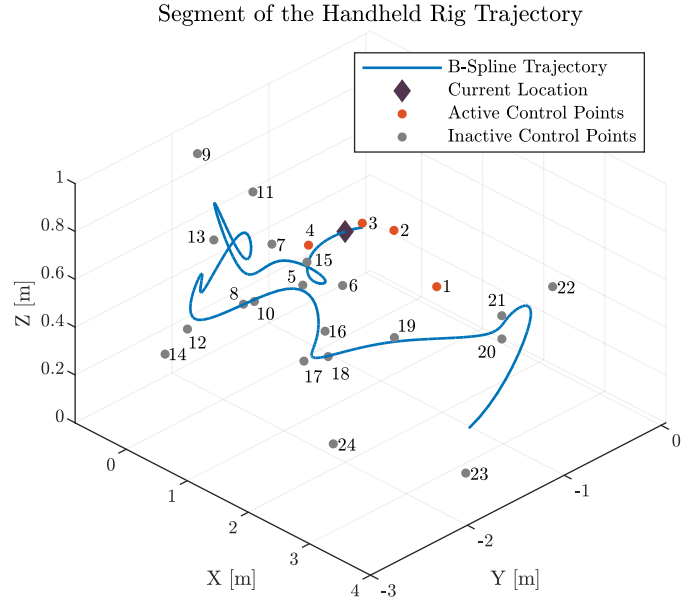


Fig. 10: A segment of the estimated  $\mathbf{r}_r^{wr}$  B-spline for the handheld rig during calibration. The purple diamond is position of the rig 6.3 s from the start of the trajectory. The active control points at 6.3 s are shown in orange. As the rig continues along the trajectory, the active nodes change.

gymnasium and an feature-rich office. For the other datasets, poor lighting conditions and rapid motions caused ORB-SLAM3 to fail. To evaluate on a given dataset, we compute the radar-camera spatiotemporal calibration parameters using our algorithm, and then run RRxIO on the same dataset with our estimated parameters. During evaluation, we disable the live ‘camera-to-IMU’ extrinsic calibration algorithm that operates as part of in RRxIO. Using the known ground truth and the estimated RRxIO trajectories, we are able to determine the quality of our calibration using the following odometry error metrics: the relative translational root mean square error (RMSE RTE), relative rotational RMSE (RRE), absolute translational RMSE (ATE), and absolute rotational RMSE (ARE).

While the parameters estimated by our algorithm are relatively close to the parameters provided in the RRxIO paper,

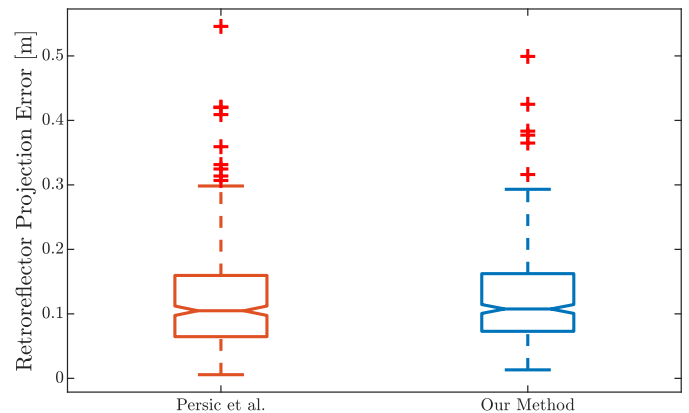


Fig. 11: The reprojection error distributions for the state-of-the-art method in [2] and ours.

TABLE II: Radar-IMU calibration parameters evaluated using three IRS datasets and RRxIO. The radar-IMU calibration parameters estimated by our algorithm are a combination of the IRS IMU-camera parameters and the camera-radar parameters we determined. The rotation between the two sensors is given in roll-pitch-yaw (i.e.,  $\theta_x, \theta_y, \theta_z$ ) Euler angle form.

	$r_x$ [cm]	$r_y$ [cm]	$r_z$ [cm]	$\theta_x$ [rads]	$\theta_y$ [rads]	$\theta_z$ [rads]	$\tau$ [ms]
RRxIO	6.00	4.00	-4.00	-3.14	0.02	-1.59	8.00
ME <sup>†</sup> (ours)	4.08	4.71	-5.05	-3.12	0.01	-1.59	13.1
MM <sup>†</sup> (ours)	3.90	4.46	-5.63	-3.11	0.01	-1.59	15.4
Gym (ours)	3.27	4.48	-3.62	-3.15	-0.06	-1.60	40.7

<sup>†</sup> These datasets are MoCap Easy (ME) and MoCap Medium (MM).

the use of our parameters result in more accurate odometry estimates. The parameters that our algorithm recovered for each dataset are shown in Table II. The estimated temporal offset for the Gym dataset is the only large deviation from the RRxIO-provided value, but, from our experience, the radar temporal offset can change significantly between system power cycles. Table III reports the absolute and relative translation and rotation errors for the RRxIO trajectories after a yaw alignment. The parameters estimated by our algorithm improve the translation error on all datasets and rotation error for two of the datasets. Notably, the Gym dataset, which has the largest temporal offset, improves the most.

TABLE III: Performance evaluation for RRxIO and our algorithm on three IRS datasets. The metrics evaluated are the relative translational RMSE (RTE), relative rotational RMSE (RRE), absolute translational RMSE (ATE), and absolute rotational RMSE (ARE).

Dataset	RTE [%]		RRE [deg/m]		ATE [m]		ARE [deg]	
	RRxIO	Ours	RRxIO	Ours	RRxIO	Ours	RRxIO	Ours
ME <sup>†</sup>	0.809	0.669	0.084	0.089	0.177	0.144	1.567	1.918
MM <sup>†</sup>	1.377	1.097	0.122	0.095	0.351	0.260	2.522	2.027
Gym	1.170	0.752	0.076	0.054	0.308	0.195	2.087	1.349

<sup>†</sup> These datasets are MoCap easy (ME) and MoCap Medium (MM).

#### D. Vehicle Experiments

In this section, we verify the accuracy of our calibration algorithm by estimating the distance between cameras mounted on an autonomous vehicle. This task was challenging because, as shown in Figure 13, the radar-camera pairs do not share overlapping fields of view, so it is impossible to perform calibration using a target-based method. Additionally, the constrained motion of the car results in a poorly conditioned problem (i.e., the minimum eigenvalue of the identifiability matrix in Equation (24) is close to zero). The poor conditioning of the problem makes the estimated parameters very sensitive to sensor measurement noise, which can lead to inaccurate results. To overcome the poor conditioning of this system, we add an extrinsic calibration prior,

$$\begin{aligned}
 \mathbf{e}_{prior} &= \log(\mathbf{T}_{cr}^{-1} \mathbf{T}_{cr,prior}), \\
 J_{prior} &= \mathbf{e}_{prior}^T \Sigma_{prior}^{-1} \mathbf{e}_{prior}, \\
 \Sigma_{prior} &= \begin{bmatrix} \sigma_t^2 \mathbf{I}_{3 \times 3} & \mathbf{0}_{3 \times 3} \\ \mathbf{0}_{3 \times 3} & \sigma_\theta^2 \mathbf{I}_{3 \times 3} \end{bmatrix},
 \end{aligned} \tag{25}$$

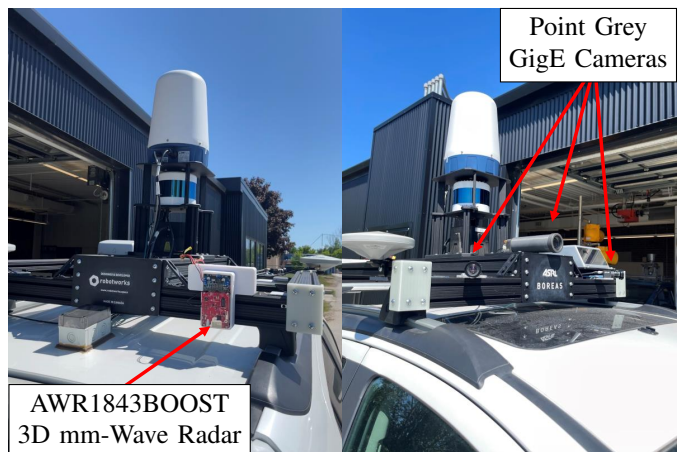


Fig. 12: Two views of the radar and camera mounting positions on the vehicle used in our experiments. The left image shows the mounting position of the TI radar. The right image shows the mounting positions of the three Point Grey cameras. The radar and the cameras do not share overlapping fields of view.

to the optimization problem. For our experiments, the prior for the extrinsic calibration parameters ( $\mathbf{T}_{cr,prior}$ ) is derived from hand measurement. We set the prior uncertainty for the translation ( $\sigma_t$ ) to 0.1 m along each axis, and the prior uncertainty for the rotation to ( $\sigma_\theta$ ) 30 degrees. The addition of this term stabilizes the estimation of the vertical translation between the radar and cameras, in particular. After optimization, less than 1% of the final cost value is due to the prior error term.

The mounting positions of the radar and three cameras on the car are shown in Figure 12, and the corresponding fields of view are shown in Figure 13. The first camera is positioned at the centre of the car and faces in the direction of travel. The two other cameras are placed to the left and to the right of the centre camera and point roughly 45 degrees from left and right from the forward axis. The 3D radar is more than one metre away from all of the cameras, facing towards the rear of the car, opposite the direction of travel.

We collected a total of nine datasets from the radar and

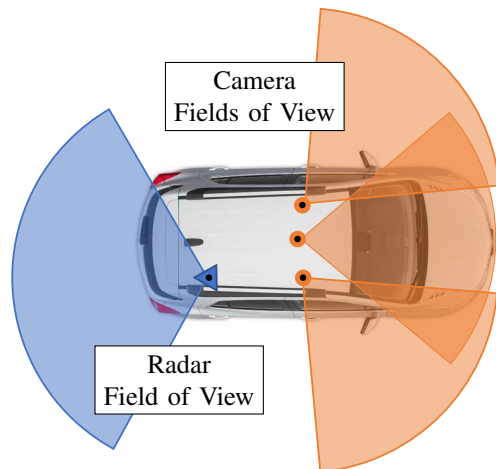


Fig. 13: Fields of view of the radar and cameras sensors used for our vehicle experiments.



the cameras (three datasets per camera) while driving two laps of a figure eight pattern. The laps occurred in a sparse parking lot environment, where the radar and camera features lie at a substantial distance from the vehicle. We evaluated the accuracy of our estimated parameters by comparing the estimated distances between the centre camera and the two side cameras to the distances measured using a Leica Nova MS50 MultiStation. This method of comparison was selected in part because camera-to-camera extrinsic calibration is difficult for camera pairs that have minimal field of view overlap. Additionally, structural components of the car prevent direct measurement of the distance between the radar and cameras. Each run of our spatiotemporal calibration algorithm produced an estimated extrinsic calibration, for a total of three sets of estimated extrinsic calibration parameters for each camera. The transformations between the centre-to-left and -right cameras are computed by combining two radar extrinsic calibration estimates, which give a total of 18 camera-to-camera extrinsic calibration estimates (nine left and nine right).

Figure 14 shows the distribution of distance errors. The majority of estimated extrinsic calibration parameters result in a camera-to-camera distance error of less than 5 cm, with two values that are greater than 10 cm. This is reasonable because we are chaining together two transforms, with translation magnitudes greater than 1 m, to confirm that the distance from the centre-to-left and -right cameras are both 35 cm.

#### E. Calibration Environment

Several notes are in order regarding environments that are suitable for calibration. Although our algorithm does not require any retroreflective targets for the radar or a specific calibration pattern for the camera, there are nonetheless some limitations on where calibration can be performed. To ensure accurate ego-velocity estimation, the calibration environment should contain, at minimum, four stationary features for ego-velocity estimation. Empirically, we have found that accurate ego-velocity estimation occurs when there are more than 10 detected features. To ensure accurate camera pose estimation using ORB-SLAM3, the scene should have sufficient lighting and visual texture. As a result, calibration should not be performed in scenes with many moving targets, dim lighting, or inclement weather (e.g., fog). However, the accuracy of the camera pose estimates are dependent on the SLAM algorithm chosen, which may or may not be robust to the previously mentioned situations.

## VII. CONCLUSION

In this paper, we described an algorithm that leverages radar ego-velocity estimates, unscaled camera pose measurements, and a continuous-time trajectory representation to perform radar-to-camera spatiotemporal calibration. We proved that the calibration problem is identifiable and determined the necessary conditions for successful calibration. Using simulation studies, we demonstrated that our algorithm is accurate, but can be sensitive to the amount of noise present in the radar range-rate measurements. Further, we evaluated our algorithm through three different, real-world experiments. First,

we showed, using data from a handheld sensor rig, that our (targetless) approach can match the accuracy of target-based calibration methods. Second, we presented results indicating that calibration can improve the localization performance of a hardware-triggered radar-camera-IMU system. Finally, we established that our calibration framework can be applied to AV systems, where the radar and camera are mounted at a significant distance from each other and do not share overlapping fields of view.

There are several potential directions for future research. It would be valuable to develop a method to automatically determine the knot spacing required for the continuous-time spline representation. Our calibration approach could be naturally extended to the multi-camera and multi-radar setting. Other pairs of sensors could also be considered beyond radar-camera pairs, including radar-inertial sensor combinations, for example.

### APPENDIX A AN EXTENSION ON THE OBSERVABILITY OF RADAR-TO-CAMERA EXTRINSIC CALIBRATION FROM WISE ET. AL [4]

In Section IV, we showed that the spatiotemporal radar-to-camera calibration problem is locally identifiable. Since the problem is locally identifiable, the batch optimization problem typically converges (unless ill-conditioned). In this appendix, we provide an extension to our earlier work in [4] demonstrating that radar-to-camera spatial calibration (with a known temporal offset) is locally weakly observable. In our observability proof, we use a different rotation representation than in Section III, which we review in Section A-A. In Section A-B, we make use of the procedure from Hermann and Krener [30] to prove that radar-to-camera extrinsic calibration is locally weakly observable. Finally, we discuss possible degenerate motions of the system, for which calibration is not possible, in Section IV-C.

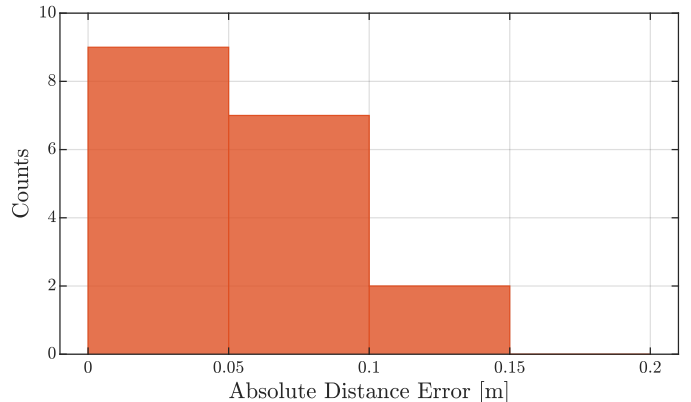


Fig. 14: Results from the vehicle calibration experiment, where the radar and the cameras do not share overlapping fields of view. The distance error is the difference between the estimated and measured distances between the center-left and center-right cameras. The ground truth distance was determined using a Leica MultiStation.



### A. Notation for Non-linear Observability Analysis

In Section III, we represent rotations using rotation matrices to define members of the Lie group  $SO(3)$ , and make use of the associated Lie algebra  $\mathfrak{so}(3)$ , which is convenient for the calibration problem but slightly more difficult to use for an observability analysis. In this section, we rely on unit quaternions to represent rotations, avoiding the need to use exponential functions. We write a unit quaternion in ‘vector’ form as

$$\mathbf{q} = [q_0 \quad \mathbf{q}_v], \quad (26)$$

with the scalar component  $q_0$  and vector component  $\mathbf{q}_v$ , such that  $\|\mathbf{q}\|_2 = 1$ . The conversion from unit quaternion to rotation matrix is given by the formula

$$\mathbf{R}_{ab} = \mathbf{R}(\mathbf{q}_{ab}) = (2q_0^2 - 1)\mathbf{I}_3 + 2\mathbf{q}_v \mathbf{q}_v^T + 2q_0 \mathbf{q}_v^\wedge. \quad (27)$$

Given the angular velocity vector  $\boldsymbol{\omega}$ , the quaternion kinematics are defined by

$$\dot{\mathbf{q}} = \frac{1}{2}\Xi(\mathbf{q})\boldsymbol{\omega} = \frac{1}{2}\Omega(\boldsymbol{\omega})\mathbf{q}, \quad (28)$$

$$\Omega(\boldsymbol{\omega}) = \begin{bmatrix} 0 & -\boldsymbol{\omega}^T \\ \boldsymbol{\omega} & -\boldsymbol{\omega}^\wedge \end{bmatrix}, \quad (29)$$

$$\Xi(\mathbf{q}) = \begin{bmatrix} -\mathbf{q}_v^T \\ q_0\mathbf{I}_3 + \mathbf{q}_v^\wedge \end{bmatrix}. \quad (30)$$

The following identity will be useful for the observability proof,

$$\frac{\partial \mathbf{R}(\mathbf{q})\mathbf{p}}{\partial \mathbf{q}} = [(4q_0\mathbf{I}_3 + 2\mathbf{q}_v^\wedge)\mathbf{p} \quad 2((\mathbf{q}_v^T \mathbf{p})\mathbf{I}_3 + \mathbf{q}_v \mathbf{p}^T - q_0\mathbf{p}^\wedge)], \quad (31)$$

where  $\mathbf{p}$  is an arbitrary  $3 \times 1$  vector. If we transpose the rotation matrix in Equation (31), then the skew-symmetric terms in Equation (31) change from positive to negative, and vice-versa.

### B. Local Weak Observability

Following the procedure outlined in Section IV-A, we define the system equations, compute the respective Lie derivatives, and demonstrate that the nonlinear observability matrix has full column rank. In the analysis here, the pose, velocity, and acceleration states of the radar-camera system are camera-centric (i.e., taken with respect to the camera and not the radar). Since the camera-centric states can be used to determine the radar-centric states, this change does not affect the observability result.

Given the camera frame  $\mathcal{F}_c$ , the world frame  $\mathcal{F}_w$ , and the radar frame  $\mathcal{F}_r$ , the state vector for the observability analysis is defined as

$$\mathbf{x} = [\mathbf{r}_w^{cwT} \quad \mathbf{q}_{wc}^T \quad \mathbf{v}_w^{cwT} \quad \boldsymbol{\omega}_c^{cwT} \quad \mathbf{a}_w^{cwT} \quad \boldsymbol{\alpha}_c^{cwT} \quad \gamma \quad \mathbf{r}_c^{rcT} \quad \mathbf{q}_{cr}^T]^T, \quad (32)$$

where  $\mathbf{r}$ ,  $\mathbf{v}$ , and  $\mathbf{a}$  denote the translation, linear velocity, and linear acceleration. The vectors  $\boldsymbol{\omega}$  and  $\boldsymbol{\alpha}$  are the angular velocity and the angular acceleration. Finally,  $\gamma$  is the scale

factor for the camera translation (for a monocular camera system). The motion model for the system is

$$\dot{\mathbf{x}} = \mathbf{f}_0(\mathbf{x}) + \mathbf{f}_1(\mathbf{x}) = \begin{bmatrix} \mathbf{0}_{3 \times 1} \\ \frac{1}{2}\Xi(\mathbf{q}_{wc})\boldsymbol{\omega}_c^{cw} \\ \mathbf{0}_{3 \times 1} \\ \boldsymbol{\alpha}_c^{cw} \\ \mathbf{0}_{3 \times 1} \\ \mathbf{0}_{3 \times 1} \\ 0 \\ \mathbf{0}_{3 \times 1} \\ \mathbf{0}_{4 \times 1} \end{bmatrix} + \begin{bmatrix} \mathbf{v}_w^{cw} \\ \mathbf{0}_{4 \times 1} \\ \mathbf{a}_w^{cw} \\ \mathbf{0}_{3 \times 1} \\ \mathbf{0}_{3 \times 1} \\ \mathbf{0}_{3 \times 1} \\ 0 \\ \mathbf{0}_{3 \times 1} \\ \mathbf{0}_{4 \times 1} \end{bmatrix}. \quad (33)$$

The measurement model equations for the (scaled) camera translation and rotation are, respectively,

$$\begin{aligned} \mathbf{h}_1 &= \gamma \mathbf{r}_w^{cw}, \\ \mathbf{h}_2 &= \mathbf{q}_{wc}. \end{aligned} \quad (34)$$

Using the camera-centric model, it is possible to directly measure  $\mathbf{q}_{wc}$  and, following Section IV-B, to determine  $\boldsymbol{\omega}_c^{cw}$  and  $\boldsymbol{\alpha}_c^{cw}$ . Finally, the radar ego-velocity measurement equation is

$$\mathbf{h}_3 = \mathbf{R}^T(\mathbf{q}_{cr})(\mathbf{R}^T(\mathbf{q}_{wc})\mathbf{v}_w^{cw} + \boldsymbol{\omega}_c^{cw\wedge}\mathbf{r}_c^{rc}). \quad (35)$$

The observability analysis requires the zeroth, first, and second order Lie derivatives. The zeroth order Lie derivatives are

$$\begin{aligned} \nabla L^0 \mathbf{h}_1 &= [\gamma\mathbf{I}_3 \quad \mathbf{0}_{3 \times 16} \quad \mathbf{r}_w^{cw} \quad \mathbf{0}_{3 \times 7}], \\ \nabla L^0 \mathbf{h}_2 &= [\mathbf{0}_{4 \times 3} \quad \mathbf{I}_4 \quad \mathbf{0}_{4 \times 20}], \\ \nabla L^0 \mathbf{h}_3 &= [\mathbf{0}_{3 \times 3} \quad \mathbf{A} \quad \mathbf{R}^T(\mathbf{q}_{cr})\mathbf{R}^T(\mathbf{q}_{wc}) \\ &\quad - \mathbf{R}^T(\mathbf{q}_{cr})\mathbf{r}_c^{rc\wedge} \quad \mathbf{0}_{3 \times 7} \\ &\quad \mathbf{R}^T(\mathbf{q}_{cr})\boldsymbol{\omega}_c^{cw\wedge} \quad \mathbf{B}], \end{aligned} \quad (36)$$

where

$$\begin{aligned} \mathbf{A} &= \mathbf{R}^T(\mathbf{q}_{cr})\frac{\partial \mathbf{R}^T(\mathbf{q}_{wc})\mathbf{v}_w^{cw}}{\partial \mathbf{q}_{wc}}, \\ \mathbf{B} &= \frac{\partial \mathbf{R}^T(\mathbf{q}_{cr})(\mathbf{R}^T(\mathbf{q}_{wc})\mathbf{v}_w^{cw} + \boldsymbol{\omega}_c^{cw\wedge}\mathbf{r}_c^{rc})}{\partial \mathbf{q}_{cr}}. \end{aligned} \quad (37)$$

The first order Lie derivatives are

$$\begin{aligned} \nabla L_{\mathbf{f}_1}^1 \mathbf{h}_1 &= [\mathbf{0}_{3 \times 7} \quad \gamma\mathbf{I}_3 \quad \mathbf{0}_{3 \times 9} \quad \mathbf{v}_w^{cw} \quad \mathbf{0}_{3 \times 7}], \\ \nabla L_{\mathbf{f}_0}^1 \mathbf{h}_2 &= [\mathbf{0}_{4 \times 3} \quad \frac{1}{2}\Omega(\boldsymbol{\omega}_c^{cw}) \quad \mathbf{0}_{4 \times 3} \\ &\quad \frac{1}{2}\Xi(\mathbf{q}_{wc}) \quad \mathbf{0}_{4 \times 14}], \\ \nabla L_{\mathbf{f}_0}^1 \mathbf{h}_3 &= [\mathbf{0}_{3 \times 3} \quad \mathbf{C} \quad \mathbf{D} \quad \mathbf{E} \quad \mathbf{0}_{3 \times 3} \\ &\quad \mathbf{F} \quad \mathbf{0}_{3 \times 1} \quad \mathbf{R}^T(\mathbf{q}_{cr})\boldsymbol{\alpha}_c^{cw\wedge} \quad \mathbf{G}], \\ \nabla L_{\mathbf{f}_1}^1 \mathbf{h}_3 &= [\mathbf{0}_{3 \times 3} \quad \mathbf{H} \quad \mathbf{0}_{3 \times 6} \\ &\quad \mathbf{R}^T(\mathbf{q}_{cr})\mathbf{R}^T(\mathbf{q}_{wc}) \quad \mathbf{0}_{3 \times 7} \quad \mathbf{L}], \end{aligned} \quad (38)$$

where

$$\begin{aligned} \mathbf{H} &= \mathbf{R}^T(\mathbf{q}_{cr})\frac{\partial \mathbf{R}^T(\mathbf{q}_{wc})\mathbf{a}_w^{cw}}{\partial \mathbf{q}_{wc}}, \\ \mathbf{L} &= \frac{\partial \mathbf{R}^T(\mathbf{q}_{cr})\mathbf{R}^T(\mathbf{q}_{wc})\mathbf{a}_w^{cw}}{\partial \mathbf{q}_{cr}}. \end{aligned} \quad (39)$$

We do not explicitly require the non-zero matrices,  $\mathbf{C}$ ,  $\mathbf{E}$ , and  $\mathbf{F}$ , in Equation (38) because the submatrix formed from the columns corresponding to the rotation states can be shown

to be full rank. The matrices  $\mathbf{D}$  and  $\mathbf{G}$  are required for the analysis, but we omit them here for brevity. The second order Lie derivatives are

$$\begin{aligned} \nabla L_{f_1}^2 \mathbf{h}_1 &= [\mathbf{0}_{3 \times 13} \quad \gamma \mathbf{I}_3 \quad \mathbf{0}_{3 \times 3} \quad \mathbf{a}_w^{cw} \quad \mathbf{0}_{3 \times 7}], \\ \nabla L_{f_0}^2 \mathbf{h}_2 &= [\mathbf{0}_{4 \times 3} \quad \frac{1}{4}(2\Omega(\boldsymbol{\alpha}_c^{cw}) - \boldsymbol{\omega}_c^{cwT} \boldsymbol{\omega}_c^{cw} \mathbf{I}_4) \\ &\quad \mathbf{0}_{4 \times 3} \quad -\frac{1}{2} \mathbf{q}_{wc} \boldsymbol{\omega}_c^{cwT} \quad \mathbf{0}_{4 \times 3} \\ &\quad \frac{1}{2} \Xi(\mathbf{q}_{wc}) \quad \mathbf{0}_{4 \times 8}]. \end{aligned} \quad (40)$$

Stacking the gradients of the Lie derivatives, we arrive at the nonlinear observability matrix,

$$\mathbf{O} = \begin{bmatrix} \nabla L^0 \mathbf{h}_1 \\ \nabla L_{f_1}^1 \mathbf{h}_1 \\ \nabla L_{f_1 f_1}^2 \mathbf{h}_1 \\ \nabla L^0 \mathbf{h}_2 \\ \nabla L_{f_0}^1 \mathbf{h}_2 \\ \nabla L_{f_0 f_0}^2 \mathbf{h}_2 \\ \nabla L^0 \mathbf{h}_3 \\ \nabla L_{f_0}^1 \mathbf{h}_3 \\ \nabla L_{f_1}^1 \mathbf{h}_3 \end{bmatrix}. \quad (41)$$

This matrix can be shown to have full column rank, and hence the system is locally weakly observable.<sup>3</sup>

### C. Degenerate Motions

Loss of identifiability will occur when  $\mathbf{O}$  in Equation (24) does not have full column rank. Wise et al. [4] presented an identifiability analysis for the radar-camera extrinsic calibration problem (i.e., without the temporal calibration extension). For completeness, we provide a more concise, extended version of a related observability proof in Appendix A. The proof in Appendix A relies on non-zero linear and angular velocities and linear accelerations, so the matrix  $\mathbf{O}$  clearly loses full rank when the radar-camera platform is not translating, rotating, or accelerating. Additionally, our earlier proof showed that the motion of the system must satisfy the following constraints to be identifiable (observable):

$$\begin{aligned} \boldsymbol{\omega}(t_2) \times \boldsymbol{\omega}(t_1) &\neq 0, \\ \mathbf{v}(t_2) \times \mathbf{v}(t_1) &\neq 0. \end{aligned} \quad (42)$$

The addition of the temporal offset to the matrix  $\mathbf{O}$  has the potential to introduce additional degenerate motions, although we have not found any thus far that would impact real-world calibration. We note that the radar ego-acceleration,  $\dot{\mathbf{v}}(t_i + \tau)$ , can be constant for all  $i$  without reducing the column rank of  $\mathbf{O}$ . We posit, based on our experiments, that degenerate motions occur infrequently in practice.

### REFERENCES

[1] C.-L. Lee, Y.-H. Hsueh, C.-C. Wang, and W.-C. Lin, "Extrinsic and Temporal Calibration of Automotive Radar and 3D Lidar," in *2020 IEEE/RSJ Intl. Conf. Intelligent Robots and Systems (IROS)*, Las Vegas, NV, USA, Oct. 25, 2020–Jan. 24, 2021 2020, pp. 9976–9983.

[2] J. Peršić, L. Petrović, I. Marković, and I. Petrović, "Spatiotemporal multisensor calibration via Gaussian processes moving target tracking," *IEEE Trans. Robotics*, vol. 37, no. 5, pp. 1401–1415, Mar. 2021.

[3] M. A. Richards, J. A. Scheer, and W. A. Holm, Eds., *Basic principles*, ser. Principles of Modern Radar. Institution of Eng. and Technol., 2010, vol. 1.

[4] E. Wise, J. Peršić, C. Grebe, I. Petrović, and J. Kelly, "A continuous-time approach for 3D radar-to-camera extrinsic calibration," in *2021 IEEE Intl. Conf. Robotics and Automation (ICRA)*, Xi'an, China, May 30–Jun. 5 2021, pp. 13 164–13 170.

[5] C. C. Stahoviak, "An instantaneous 3D ego-velocity measurement algorithm for frequency modulated continuous wave (FMCW) doppler radar data," Master's thesis, University of Colorado at Boulder, 2019.

[6] S. Sugimoto, H. Tateda, H. Takahashi, and M. Okutomi, "Obstacle detection using millimeter-wave radar and its visualization on image sequence," in *Int. Conf. Pattern Recognition (ICPR)*, Cambridge, England, Aug. 23–26 2004, pp. 342–345.

[7] T. Wang, N. Zheng, J. Xin, and Z. Ma, "Integrating millimeter wave radar with a monocular vision sensor for on-road obstacle detection applications," *Sensors*, vol. 11, no. 9, pp. 8992–9008, Sep. 2011.

[8] D. Y. Kim and M. Jeon, "Data fusion of radar and image measurements for multi-object tracking via Kalman filtering," *Information Sciences*, vol. 278, pp. 641–652, Sep. 2014.

[9] J. Kim, D. S. Han, and B. Senouci, "Radar and vision sensor fusion for object detection in autonomous vehicle surroundings," in *2018 4th Int. Conf. Ubiquitous and Future Networks (ICUFN)*, Prague, Czech Republic, Jul. 3–6 2018, pp. 76–78.

[10] T. Kim, S. Kim, E. Lee, and M. Park, "Comparative analysis of RADAR-IR sensor fusion methods for object detection," in *2017 17th Int. Conf. Control, Automation and Systems (ICCAS)*, Jeju, Korea, Oct. 18–21 2017, pp. 1576–1580.

[11] G. El Natour, O. Ait Aider, R. Rouveure, F. Berry, and P. Faure, "Radar and vision sensors calibration for outdoor 3D reconstruction," in *2015 IEEE Int. Conf. Robotics and Automation (ICRA)*, Seattle, WA, USA, May 25–30 2015, pp. 2084–2089.

[12] J. Domhof, J. F. P. Kooij, and D. M. Gavrilu, "An extrinsic calibration tool for radar, camera and lidar," in *2019 Int. Conf. Robotics and Automation (ICRA)*, Montréal, Canada, May, 20–24 2019, pp. 8107–8113.

[13] J. Peršić, I. Marković, and I. Petrović, "Extrinsic 6DoF calibration of a radar–lidar–camera system enhanced by radar cross section estimates evaluation," *Robotics and Autonomous Systems*, vol. 114, pp. 217–230, Apr. 2019.

[14] J. Oh, K. Kim, M. Park, and S. Kim, "A comparative study on camera-radar calibration methods," in *2018 15th Int. Conf. Control, Automation, Robotics and Vision (ICARCV)*, Singapore, Nov. 18–21 2018, pp. 1057–1062.

[15] C. Schöller, M. Schnettler, A. Krämmer, G. Hinz, M. Bakovic, M. Güzet, and A. Knoll, "Targetless rotational auto-calibration of radar and camera for intelligent transportation systems," in *2019 IEEE Intelligent Transportation Systems Conf. (ITSC)*, Auckland, New Zealand, Oct. 27–30 2019, pp. 3934–3941.

[16] J. Peršić, L. Petrović, I. Marković, and I. Petrović, "Online multi-sensor calibration based on moving object tracking," *Advanced Robotics*, vol. 35, no. 3–4, pp. 130–140, Sep. 2021.

[17] L. Heng, "Automatic targetless extrinsic calibration of multiple 3D lidars and radars," in *2020 IEEE/RSJ Intl. Conf. Intelligent Robots and Systems (IROS)*, Las Vegas, NV, USA, Oct. 25, 2020–Jan. 24, 2021 2020, pp. 10 669–10 675.

[18] D. Kellner, M. Barjenbruch, K. Dietmayer, J. Klappstein, and J. Dickmann, "Joint radar alignment and odometry calibration," in *2015 18th Int. Conf. Information Fusion (FUSION)*, Washington, DC, USA, Jul. 6–9 2015, pp. 366–374.

[19] C. Doer and G. F. Trommer, "Radar inertial odometry with online calibration," in *2020 European Navigation Conf. (ENC)*, Nov. 23–24 2020, pp. 1–10.

[20] J. Rehder, R. Siegwart, and P. Furgale, "A general approach to spatiotemporal calibration in multisensor systems," *IEEE Trans. Robotics*, vol. 32, no. 2, pp. 383–398, Apr. 2016.

[21] T. D. Barfoot, *State estimation for robotics*. Cambridge, UK: Cambridge Univ. Press, 2017.

[22] C. Sommer, V. Usenko, D. Schubert, N. Demmel, and D. Cremers, "Efficient derivative computation for cumulative B-splines on Lie groups," in *2020 IEEE/CVF Conf. Computer Vision and Pattern Recognition (CVPR)*, Jun. 14–19 2020, pp. 11 145–11 153.

[23] C. de Boor, *A Practical Guide to Splines*. Springer-Verlag, Jan. 1978, vol. 27.

[24] K. Qin, "General matrix representations for b-splines," in *6th Pacific Conf. on Computer Graphics and Applications*, Singapore, Oct. 26–29 1998, pp. 37–43.

<sup>3</sup>We omit the full derivation for brevity, and note that the rank condition can be verified in this case using any symbolic algebra package.

- [25] C. Doer and G. F. Trommer, "An EKF based approach to radar inertial odometry," in *2020 IEEE Intl. Conf. Multisensor Fusion and Integration for Intelligent Systems (MFI)*, Karlsruhe, Germany, Sep. 14–16 2020, pp. 152–159.
- [26] A. Chiuso, P. Favaro, Hailin Jin, and S. Soatto, "Structure from motion causally integrated over time," *IEEE Trans. Pattern Analysis and Machine Intelligence*, vol. 24, no. 4, pp. 523–535, Apr. 2002.
- [27] S. Agarwal *et al.*, *Ceres Solver*. [Online]. Available: <http://ceres-solver.org>
- [28] M. Li and A. I. Mourikis, "Online temporal calibration for camera-IMU systems: Theory and algorithms," *Intl. J. Robotics Research*, vol. 33, no. 7, pp. 947–964, 2014.
- [29] R. A. Hewitt and J. A. Marshall, "Towards intensity-augmented SLAM with LiDAR and ToF sensors," in *Proc. IEEE/RSJ Intl. Conf. Intelligent Robots and Systems (IROS)*, Hamburg, Germany, September/October 2015, pp. 1957–1961.
- [30] R. Hermann and A. Krener, "Nonlinear controllability and observability," *IEEE Trans. Automatic Control*, vol. 22, no. 5, pp. 728–740, Oct. 1977.
- [31] J. Kelly, C. Grebe, and M. Giamou, "A question of time: Revisiting the use of recursive filtering for temporal calibration of multisensor systems," in *Proc. IEEE Intl. Conf. Multisensor Fusion and Integration (MFI)*, Karlsruhe, Germany, 2021.
- [32] C. Doer and G. F. Trommer, "Radar visual inertial odometry and radar thermal inertial odometry: Robust navigation even in challenging visual conditions," in *2021 IEEE/RSJ Intl. Conf. Intelligent Robots and Systems (IROS)*, Prague, Czech Republic, Sep. 27 – Oct. 1 2021, pp. 331–338.
- [33] K. Burnett, D. J. Yoon, Y. Wu, A. Z. Li, H. Zhang, S. Lu, J. Qian, W.-K. Tseng, A. Lambert, K. Y. Leung, A. P. Schoellig, and T. D. Barfoot, "Boreas: A multi-season autonomous driving dataset," *The International Journal of Robotics Research*, vol. 0, no. 0, p. 02783649231160195, 2023.
- [34] Texas Instruments, *xWR1843 Evaluation Module (xWR1843BOOST) Single-Chip mmWave Sensing Solution*, May 2020. [Online]. Available: <https://www.ti.com/lit/ug/spruim4b/spruim4b.pdf>
- [35] —, *IWR6843AOP Single-Chip 60- to 64-GHz mmWave Sensor Antennas-On-Package (AOP)*, July 2022. [Online]. Available: <https://www.ti.com/lit/ds/symlink/iwr6843aop.pdf>
- [36] C. Campos, R. Elvira, J. J. G. Rodríguez, J. M. M. Montiel, and J. D. Tardós, "ORB-SLAM3: An accurate open-source library for visual, visual-inertial, and multimap SLAM," *IEEE Trans. Robotics*, vol. 37, no. 6, pp. 1874–1890, May 2021.
- [37] E. Olson, "AprilTag: A robust and flexible visual fiducial system," in *2011 IEEE Intl. Conf. Robotics and Automation (ICRA)*, Shanghai, China, May 9–13 2011, pp. 3400–3407.



**Jonathan Kelly** received the Ph.D. degree in Computer Science from the University of Southern California, Los Angeles, USA, in 2011. From 2011 to 2013 he was a postdoctoral associate in the Computer Science and Artificial Intelligence Laboratory at the Massachusetts Institute of Technology, Cambridge, USA. He is currently an associate professor and director of the Space and Terrestrial Autonomous Robotics Systems (STARS) Laboratory at the University of Toronto Institute for Aerospace Studies, Toronto, Canada. Prof. Kelly holds the Tier II Canada Research Chair in Collaborative Robotics. His research interests include perception, planning, and learning for interactive robotic systems.



**Emmett Wise** received his Bachelor of Applied Science in engineering physics from Queens University, Kingston, Canada, in 2016. After graduation, he worked to automate the manufacturing of nanoscale coatings at 3M Canada. He is currently a Ph.D. Candidate in the Space and Terrestrial Autonomous Robotics (STARS) Laboratory at the Institute for Aerospace Studies, Toronto, Canada. His research interests include perception, calibration, and state estimation.



**Qilong (Jerry) Cheng** is currently pursuing his Bachelor of Applied Science degree in mechanical engineering at the University of Toronto. He was a developer at Autodesk from 2019 to 2020. From 2020 to 2021, he made contributions to a high pressure spray nozzle design for the China State Shipbuilding Corporation. He is currently an undergraduate research student in the Space and Terrestrial Autonomous Robotics (STARS) Laboratory at the University of Toronto, focusing on calibration and state estimation.